Chaos, Solitons and Fractals 172 (2023) 113615

Contents lists available at ScienceDirect

Chaos, Solitons and Fractals

journal homepage: www.elsevier.com/locate/chaos

Identification of weakly to strongly-turbulent three-wave processes in a micro-scale system

J. Orosco, W. Connacher, J. Friend *

Medically Advanced Devices Laboratory, Center for Medical Devices, Department of Mechanical and Aerospace Engineering, Jacobs School of Engineering and Department of Surgery, School of Medicine, University of California San Diego, La Jolla, CA 92093-0411, USA

ARTICLE INFO

Keywords:
Wave turbulence
Kinetic theory
Microfluidics
Ultrasound
Interfacial dynamics

ABSTRACT

We find capillary wave turbulence (WT) spanning multiple dynamical regimes and geometries, all within a 40 μL volume microfluidic system. This study is made viable with recent advances in ultra-high-speed digital holographic microscopy, providing 10 μs time and 10 nm spatial resolutions for images across the entire field at speeds sufficient to capture the salient wave phenomena. The observed WT types are: (i) discrete wave turbulence (DWT) dominated by finite domain effects, (ii) kinetic wave turbulence (KWT) that approximately satisfies weak wave turbulence (WWT) theory, and (iii) intermediate wave turbulence (IWT) that exhibits features from both DWT and KWT. We show that WT regime depends on input power and wavenumber, and we provide simple nondimensional parameters – derived from WWT theory – for intra-spectrum regime classification. Using the nondimensional parameters, a bulk nonlinearity metric is defined that employs bicoherence-based weighting. Analysis of experimental results reveals a correspondence between the theoretical regime classifiers and the observed phenomena. At sufficiently high input powers, the phenomena substantially depart from the WWT theory and reveal a regime of strongly nonlinear wave turbulence (SWT) defined by shallower spectral slopes that achieve a constant slope value over a range of input powers. This may suggest a corresponding power-law solution to the governing equations. This work augments current understanding of WT regimes and behaviors, and directly applies to many fields beyond fluid mechanics. For example, SWT appears upon the fluid interface at powers less than required for atomization, indicating that further study of SWT is needed to properly understand ultrasound-driven fuel spray atomization and drug and agricultural nebulization.

1. Introduction

Applications from ink jet printing to fuel combustion depend on rapid, monodisperse droplet production [1,2]. Many depend on atomization to produce micron-sized droplets from small fluid volumes [3]. Leveraging enormous acceleration, high-frequency ultrasound (HFUS) at 1 MHz and beyond extends the utility of ultrasound-driven atomization to broader fluid parameter ranges. The phenomena are poorly understood and even basic predictions – such as droplet diameter and ejection rate – remain elusive. In particular, classical interpretations of ultrasound-driven atomization [4–7] that rely on sophisticated modeling [8–11] produce inaccurate estimates at frequencies beyond 100 kHz. More recent, ad-hoc approaches produce interesting results but remain insufficient [12,13]. In fact, classical mechanisms of acoustically-driven interfacial wave generation used even to recent times [14–17] are absent in MHz-order HFUS-driven wave fields [18].

A top-down understanding of the relationship between the wave field and droplet statistics is desirable for navigating these theoretical challenges. Highly stochastic, generally non-Gaussian turbulent capillary wave fields preceding aerosol dispersal are a key source of theoretical ambiguity. When forcing magnitudes are increased above a threshold, low-frequency linear mode superpositions give way to energy cascades across essentially continuous wavenumber distributions [18–20]. The hallmark of this turbulent cascade is a well-defined, monotonically decreasing, non-integer linear slope in the log–log PSD.

Wave turbulence (WT) is of great general interest arising in diverse contexts, from brain activity patterns [21] to optical wave propagation within nonlinear media [22]. In pioneering work, Zakharov and Filonenko [23] derived a kinetic equation – at third order in wave amplitudes – governing capillary WT cascades in unbounded basins by expanding the interfacial dynamics Hamiltonian. This equation governs conservative dynamics from the "inertial" range down to the beginning

* Corresponding author.
E-mail address: jfriend@ucsd.edu (J. Friend).

https://doi.org/10.1016/j.chaos.2023.113615
Received 25 January 2023; Received in revised form 9 April 2023; Accepted 22 May 2023
Available online 7 June 2023

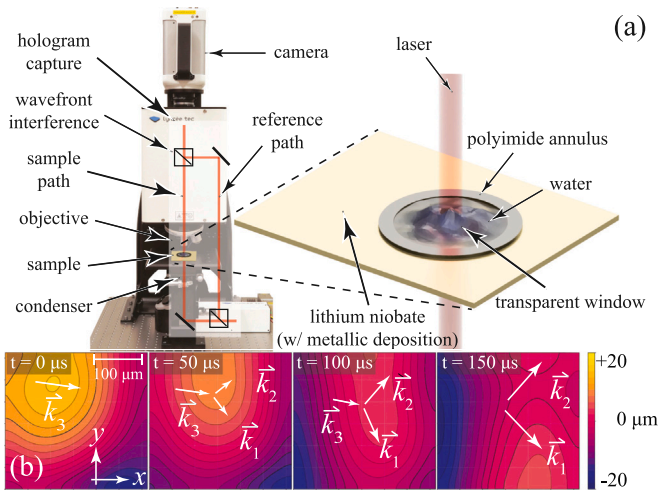

Fig. 1. High-speed digital holographic microscopy of turbulent microscale capillary waves. (a): An interferometer using a 666 nm laser expanded to occupy the entire field of view of the optics produces phase and intensity patterns that encode 3D surface data recorded at 115.2 kfps. A 25 × 20 × 0.5 mm piezoelectric transducer, with a 6.4 mm window in the electrodes allowing laser passage, is driven at its resonant frequency of 7 MHz, causing vibration below a 725 μm deep fluid volume contained by a 9.5 mm diameter annulus. (b) Four frames from a typical holographic data set of interfacial dynamics depicts a typical three-wave interaction.

of the viscous "dissipation" range. They showed that the stationary collision integral identity is satisfied by $n(k) \propto k^{-\gamma}$, where n is proportional to the square of the wave amplitude at wavenumber k. The system in Ref. [23] has $\gamma = 17/4$. Due to the governing kinetic equation, this is denoted "kinetic" WT (KWT). Strong WT (SWT), by contrast, is WT violating the weak nonlinearity assumption.

Within finite geometries, WT behaviors deviate substantially from the idealizations inherent to KWT. Wavemodes form a countable set and are designated "discrete" WT (DWT). Kartashova [24] shows that exact three-wave equations satisfied in capillary KWT become Diophantine in DWT and are equivalent to $x^3 + y^3 = z^3$, which has no solutions (*see* Fermat's Last Theorem [25]). In such an absence of exact resonances, waves build to finite amplitudes, invoking higher order terms in the nonlinear dispersion relations [26,27] and leading to quasi-resonant three-wave relations [28]:

$$|\omega_{k_1} \pm \omega_{k_2} - \omega_{k_3}| \leq \delta_{\mathrm{NRB}}, \tag{1a}$$

$$\mathbf{k}_1 \pm \mathbf{k}_2 - \mathbf{k}_3 = 0, \tag{1b}$$

where $\omega_{k_n} \triangleq \omega(\mathbf{k}_n)$. The parameter δ_{NRB} represents nonlinear resonance broadening (NRB) resulting from the finite-amplitude dispersion relation. In unbounded media, $\delta_{\mathrm{NRB}} = 0$ and exact resonances appear as arguments to Dirac combs within a collision integral kernel. In finite media, δ_{NRB} builds to finite values so that the equations are satisfied by groupings of quasiresonances about exact modes. Modal broadening facilitates additional wave interactions and eventual turbulent breakdown.

When δ_{NRB} values are relatively small, the energy cascade is arrested and confined to smaller wavenumbers. This confinement is a phenomenon that some authors refer to as "frozen" turbulence [27]. Connaughton et al. [28] have predicted the existence of a critical NRB value beyond which cascades indefinitely advance. The mechanism of cascade advancement from larger forcing – a phenomenon that some authors refer to as "sandpiling" – has been described by Nazarenko [29]. In real systems, DWT and KWT coexist [27,30–33]. The dominance of either mechanism depends on wavenumber and forcing amplitude and can be classified as follows: (i) at low powers and/or small wavenumbers, DWT dominates; (ii) at high powers and/or large wave numbers, KWT dominates; and (iii) at intermediate powers and/or intermediate wavenumbers: a combination of DWT and KWT contribute to observations. We designate condition (iii) as intermediate WT (IWT). Other authors have referred to this as "mesoscopic" WT [32].

The majority of liquid WT experiments are devoted to gravity waves of the type found on sea surfaces [34]; surface tension-dominant systems – capillary waves – receive comparatively little attention. Work that *has* considered capillary waves generally takes place in deep water environments, often in the presence of gravity waves, and focuses on regimes where kinetic theory is approximately satisfied. Brazhnikov et al. [35] studied capillary wave turbulence on an air–water interface with low-frequency pumping [$\mathcal{O}(10^2)$ Hz] leading to a turbulent cascade with a power law, $\gamma = 17/4$, that agrees with Zakharov's prediction. Using a capacitive technique, Falcon et al. [36] measured capillary–gravity wave turbulence on the surface of a mercury pool driven with $\mathcal{O}(10^1)$ Hz forcing. They found non-Gaussian wave statistics and spectral slopes that agree with WWT theory for each interaction type (four-wave for gravity and three-wave for capillary) within corresponding wavenumber ranges. In a similar work, Xia et al. [19] studied the formation of capillary wave turbulence, observing modal broadening and a transition from discrete to continuous wavemode spectra as a result of the theorized modulation instability. They also confirmed Zakharov's slope prediction within a fully developed turbulent capillary wave field. Other studies have similarly sought to study various aspects predicted by the WWT theory, focusing primarily on KWT [37–39]. All of these are a result of the classical Faraday wave system where a cascade (the "inertial" region) joins a small-wavenumber injection range to a large-wavenumber dissipation range. In contrast to KWT, explicit consideration of finite-domain effects and DWT has remained mostly theoretical, with Pan and Yue [40] recently providing an elegant framework to account for discreteness by extending earlier work in the kinetic theory of deep-water capillary waves [41,42]. Here, we study a surface tension-dominated system where spatial scales are much smaller than the capillary length, $k_*^{-1} = \sqrt{\sigma/\rho g}$, so that the effect of gravity is negligible. The waves are driven using a range of HFUS forcing that generates wavefields demonstrating all WT regimes, from DWT to KWT. With sufficiently strong forcing, we observe energy cascades in a strongly nonlinear regime with power-law spectral slopes that depart from those defining the associated WWT theory for KWT. In these systems, injection occurs at a much higher frequency than the dissipation range, so that these are not classical Faraday systems. The device geometry used in our experiments approximates the dimensions of moderately shallow, surface-wetting "puddles" that form on prototype portable ultrasonic nebulizers developed in our lab [43] (*see* [supplemental materials]). As such, the observed spectra represent wavemodes that occur within a mixture of shallow, intermediate, and deep water depths. We can access these dynamics due to microsecond-nanometer resolutions provided by our custom ultra high-speed (UHS) digital holographic microscope (DHM) [44]. Without this capability, relevant portions of the cascade would be unreachable. Summarizing, the associated data pass through several quantitatively-significant physical regimes due to the range of scales, geometries, and wavenumbers we considered: (i) basin depth: shallow, intermediate, and deep; (ii) dominant WT dynamics: discrete, intermediate, and kinetic; and (iii) nonlinearity level: weak and strong. To aid in the analysis and classification of the turbulent wave systems, we derive dimensionless quantities from discrete and kinetic theory.

2. Experiment

The experimental configuration is outlined in Fig. 1. The device is a 25 mm × 20 mm × 0.5 mm single-crystal, transparent lithium niobate piezoelectric transducer with electrodes deposited on each face leaving a 6.35 mm diameter window. In order to repeatably produce a fluid sample upon this substrate, a 60 μm thick polyimide annulus with inner diameter 9.5 mm was affixed to the top face, encircling the window.

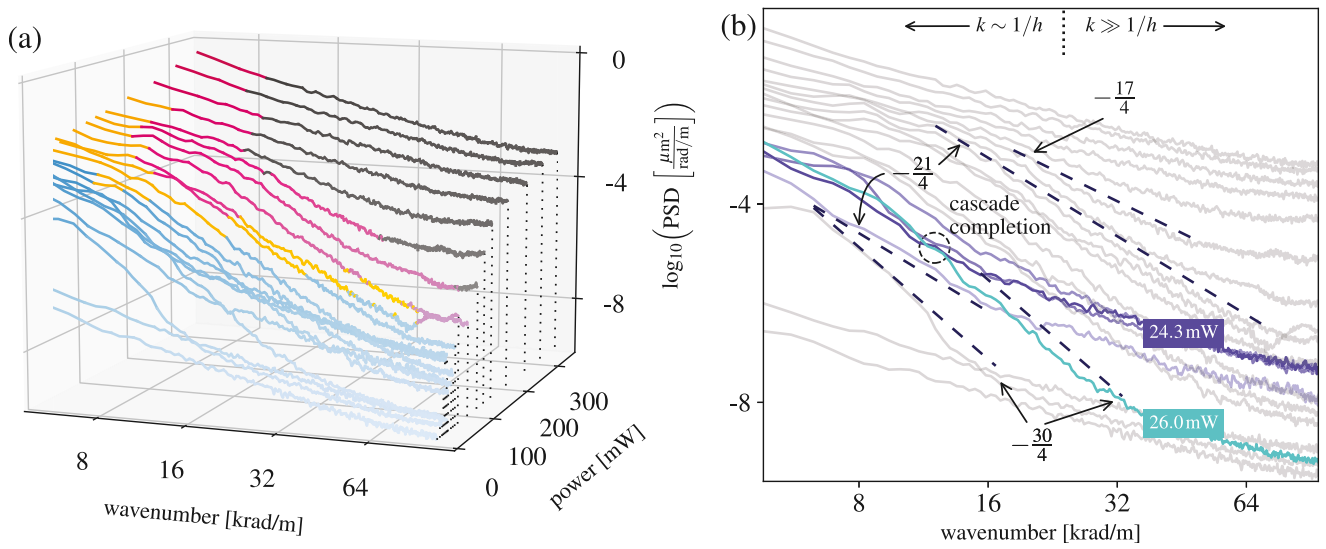

Fig. 2. Turbulent micro capillary wave power spectral density regime classification. (a) The measured power spectral density, plotted with respect to wavenumber as functions of increasing power may be classified in terms of their WT regimes: (blue) discrete, (yellow) intermediate, (pink) kinetic, and (gray) strong. The first three are defined in Eqs. (6) and (9). The fourth is discussed later and demonstrated in Fig. 3. (b) An input of 24.3 mW leads to an arrested cascade. Increasing the power to 26 mW leads to cascade completion, demonstrating a critical NRB value as theorized in Ref. [28]. Also shown (light to dark purple lines) are three input powers preceding 24.3 mW: 15.5 mW, 18.5 mW, and 21.5 mW. The indicated slopes are 17/4, the kinetic capillary wave slope predicted by Zakharov [23]; the steepest slope, 21/4, observed in simulations of Ref. [40] and corresponding to an approximately constant slope over the KWT regime here (as discussed later); and the steepest slope, 30/4, observed in our experiments, both at capillary wave onset and immediately after the critical NRB value for a 26 mW input. Spectra in these plots are generated using Welch's method with Hann windowing and fifty percent overlap to average roughly one hundred spectra for all but the lowest two powers (0 and 7 mW). The shallow regime (not shown) exists at wavenumbers $\lesssim 2$ krad/m. A detailed description of what is meant by "arrested cascade", "cascade completion", and "critical NRB value" is provided in the main text. (For interpretation of the references to color in this figure legend, the reader is referred to the web version of this article.)

Deionized water (40 μL) was pipetted into the annulus such that a thin circular lens with maximum central depth ≈ 725 μm completely filled the polyimide annulus, placing the contact line at the top edge of the annulus. A sinusoidal voltage signal was applied at 7.001 MHz, driving the fundamental thickness-mode resonance in the transducer [45]. Greater detail regarding materials, fabrication, and characterization is available in [supplemental materials].

The central portion of the air–water interface was then imaged using an UHS camera (Photron, SA-Z) coupled to a DHM (Lynceé Tec SA, Lausanne, Switzerland) with custom optics designed by Lynceé Tec SA for these experiments. High-intensity coherent light from a 666 nm laser is equally split between measurement light passing through the sample and reference light passed unhindered around the sample. Light passing through the sample medium encounters a phase delay with respect to the reference. Using the sample's refractive index, the phase delay may be associated with a displacement up to $2\pi\lambda$ where λ is the light source's wavelength. Phase jumps exist at integer multiples of $2\pi\lambda$; left unaccounted for, they create ambiguity in predictions of the displacement of the sample's medium. However, if the height gradually changes with respect to the viewing plane, phase jumps that occur can be *unwrapped* – accounted for – to produce high-fidelity surface displacement measurements well beyond the $2\pi\lambda$ limit. These measurements take the form of phase-intensity images of the viewable surface called "holograms". We obtained surface holograms covering a 300 μm × 300 μm square central region of the oscillating fluid interface. Holograms were recorded at 115.2 kfps with a 10 nm displacement resolution along the light propagation direction, and a 1.2 μm lateral image plane resolution. The curated data (300 GB) obtained for this study are freely provided for download [46].

3. Classifying wave turbulence regimes

We analyze the experimental results from two perspectives: (i) intra-spectrum classification: which permits wavenumber-dependent analysis within a given experimental run, and (ii) global nonlinearity analysis: which associates a single value with the nonlinearity for a given experimental run.

3.1. Intra-spectrum regime classification

We use an approach similar to Zakharov [47] and L'vov and Nazarenko [30] to facilitate intra-spectrum analysis. They compared the nonlinear resonance broadening (NRB), δ_{NRB}, to the frequency spacing, δ_k, in the eigenmode grid that is imposed by the finite geometry. DWT dominates the wavemode behavior when $\delta_{\mathrm{NRB}} \ll \delta_k$. KWT dominates the wavemode behavior when $\delta_{\mathrm{NRB}} \gg \delta_k$. Otherwise, the characteristics of both types may be observed, leading to IWT. Their quantification of NRB is derived from WWT theory (*see* [supplemental materials]). In other words, when resonances have been sufficiently broadened, the injected energy can more easily traverse the eigenmode grid from small to large wavenumbers, leading to fully-developed, well-defined WT cascades.

With this approach in mind, we derive and apply dimensionless parameters to quantitatively classify WT regimes observed in our surface measurements. In addition to aiding in the classification of experimental observations, these parameters also help to identify the appropriate approach to later use in analysis of the wave phenomena. For example, when DWT dominates, resonance conditions are Diophantine equations (*i.e.*, algebraic equations defined over integers), and therefore rigorous analysis may require a number theoretical approach [24].

The appropriate formulation of the NRB depends on the wave turbulent regime being analyzed, with NRB in KWT expressed via the kinetic equation and NRB in DWT expressed via the discrete equations of motion [*see* supplemental materials]. Each of these is associated with the collision integral kernel localized to the particular wavenumber being considered and represent the coupling strength applied to a broadened (by NRB) Delta function condition. In the case of DWT, a characteristic broadening depends on the number of exact resonances, $\mathcal{N}_k$, that are numerically significant at a fixed wavenumber, as discussed below (consult Ref. [30] for greater detail). The NRB parameter is given for these two cases by [30]

$$\delta_{\mathrm{NRB}} = \begin{cases} |V_k\, a_k|\, \mathcal{N}_k, & \text{(DWT)} \\ |V_k|^2 |a_k|^2 (k\,L)^2/\omega_k, & \text{(KWT)} \end{cases} \tag{2}$$

where $|(\cdot)|$ denotes the complex modulus. The parameter V_k is a simplified approximation of the interaction coefficient; it only depends upon the wavenumber. The canonical amplitude variable a_k is related to the Fourier amplitude [27]:

$$\zeta_k = \sqrt{\frac{\rho\,\omega_k}{2\,\sigma\,k^2}}(a_k + a^*_{-k}), \tag{3}$$

where σ is the interfacial surface tension and ρ is the fluid density. Note that Eq. (3) assumes normalization of the Fourier transform by $\sqrt{2\,\pi}$. For the capillary wave systems we consider here, wavenumber locality is assumed in the resonance interactions – that is, $k_1 \sim k_2 \sim k_3$ – so that $\mathcal{N}_k \gtrsim 1$ is a reasonable approximation. We set $\mathcal{N}_k = 1$ for an order-of-magnitude analysis in order to avoid unnecessary complexity. Deviations of $\mathcal{N}_k$ that remain approximately within an order of magnitude do not significantly impact the analysis and classification that follows.

The particular forms of the dispersion relation and the interaction coefficient depend on the depth of the fluid. They determine the form our classification parameters ultimately take for a given data set. Our system progresses from shallow at wavenumbers of $\mathcal{O}(10^2)$ rad/m to deep at wavenumbers of $\mathcal{O}(10^4)$ rad/m. Intermediate regimes are defined by interpolating between the shallow and deep conditions (*see* [supplemental materials]), and formulations for both asymptotic regimes (shallow and deep) are therefore needed.

3.1.1. Shallow water classification ($k_* \ll k \ll 1/h$)

The shallow water capillary wave dispersion relation is

$$\omega_k = \sqrt{\frac{\sigma\,h}{\rho}}k^2. \tag{4}$$

The interaction coefficient for shallow water waves is [48]

$$V_k = \frac{k^2}{8\,\pi}\left(\frac{\sigma}{4\,\rho\,h}\right)^{1/4}. \tag{5}$$

Combining Eqs. (2)–(5) and accounting for eigenmode grid spacing as noted in [supplemental materials], we produce the following shallow-water WT regimes:

$$\text{DWT} \quad \text{if} \quad \Delta_s = \tfrac{1}{16\,\pi}\mathcal{A}_v/\mathcal{A}_w \ll 1, \tag{6a}$$

$$\text{KWT} \quad \text{if} \quad \Lambda_s = 2\,\pi^2\,S_w\,\Delta_s^2 \gg 1, \tag{6b}$$

$$\text{IWT} \quad \text{otherwise}, \tag{6c}$$

where $\mathcal{A}_w = \frac{1}{k\,\hat{\zeta}_k}$ is the wave aspect ratio, $\mathcal{A}_v = \frac{1}{k_m\,h}$ is the quiescent fluid volume aspect ratio, and $\hat{\zeta}_k$ is the Fourier-transformed wave amplitude. Referring to Fig. 1, the grid spacing is $k_m = \pi/D_{\text{inner}}$. We define the wave seclusion as $S_w = k/k_m$. This parameter represents the extent to which a wavemode is affected by the boundary conditions, with $S_w \gg 1$ indicating negligible boundary effects and the inverse indicating significant boundary effects. Note that we have retained any constant factors (*e.g.*, $16\,\pi$) in the derived nondimensional expressions in keeping with our order-of-magnitude analysis.

Essentially, the condition for shallow water DWT is that the quiescent fluid should be much deeper (relative to its own breadth) than the waves are tall (relative to their own wavelength). For KWT, the opposite should be true, and the waves should be isolated from boundary effects.

3.1.2. Deep water classification ($k \gg 1/h$)

The deep water capillary wave dispersion relation is

$$\omega_k^2 = \frac{\sigma}{\rho}k^3. \tag{7}$$

By using our previously noted assumption of wavenumber locality and performing an order-of-magnitude analysis, we approximate the interaction coefficient [27] for capillary waves in deep water:

$$V_k \approx \frac{1}{8\,\pi}\sqrt{\frac{\rho\,\omega_k^3}{2\,\sigma}}. \tag{8}$$

Combining Eqs. (2)–(3), and (7)–(8) and accounting for eigenmode grid spacing as noted in [supplemental materials], we obtain the following deep-water WT regimes:

$$\text{DWT} \quad \text{if} \quad \Delta_d = \tfrac{1}{12\,\pi}S_w/\mathcal{A}_w \ll 1, \tag{9a}$$

$$\text{KWT} \quad \text{if} \quad \Lambda_d = \tfrac{3\,\pi^2}{2}S_w\,\Delta_d^2 \gg 1, \tag{9b}$$

$$\text{IWT} \quad \text{otherwise}. \tag{9c}$$

Thus, in deep water only the lateral dimension is relevant, whereas in shallow water (Eq. (6)) the definition of the regimes depend on both dimensions. For deep water, finite-basin effects occur when the a given wave's steepness is large relative to the boundary effects on that wave. Moreover, in deep water, the KWT condition has weaker wave-boundary seclusion requirements and stronger wave steepness requirements. This qualitatively agrees with expressions found elsewhere in the literature [29,49]. Eqs. (6) and (9) and the wave turbulence regimes they define depend upon the wavenumber. Fundamentally, the wave turbulence regimes are *geometrically determined*. In other words, the variables used in these formulations are based on the relative geometries of the wave and the fluid domain.

3.1.3. Intra-spectrum analysis

We can use the foregoing nondimensional parameters in order to approximately demarcate wave turbulence regimes within the spectrum of a given set of measurements (*i.e.*, for a given power input). Fig. 2 outlines the spectral features of our system written in terms of power spectra, S. In shallow regions, $S_{\text{D-I}} \propto k^{-2}$ and $S_{\text{I-K}} \propto k^{-3}$, respectively, for the DWT-IWT (D-I) and the IWT-KWT (I-K) PSD bounds. In deep regions, $S_{\text{D-I}} \propto k^{-4}$ and $S_{\text{I-K}} \propto k^{-5}$. The change is a consequence of the continuously increasing effect of δ_{NRB} within the finite-depth basin as energy is redistributed to larger wavenumbers in the cascade. In the intermediate regime between shallow and deep wavenumbers, the change in the regime bounds (*i.e.*, the variation between asymptotic definitions) – which are proxies for the character of the WT – will smoothly and monotonically vary, joining the two extremes. Mathematically, this regime is represented by interpolation as described in [supplemental materials].

Detailed inspection of these spectra reveals order-of-magnitude agreement of regime bounds with expected spectral characteristics. Theoretically, the hallmark of DWT is arrested cascades that are incrementally extended as NRB increases, allowing energy transfer to larger wavenumbers (as previously discussed) [29]. Departure from the expected uniform linearity of the cascade leads to an irregular lumpy appearance in the spectral shapes visible at lower input powers ($P \lesssim 24\,\text{mW}$) in Fig. 2. This indicates energy confinement at smaller wavenumbers due to insufficient NRB allowing complete energy transfer to larger wavenumbers: cascade arrest. This manner of spectral volatility defines the DWT regime. As the power is increased towards the DWT-IWT boundary, the shape and amplitude of the spectra remain approximately constant until NRB overcomes the discrete modal separation, as theorized by Connaughton et al. [28]. Beyond this threshold power defined by the characteristics of the system – $P \gtrsim 26\,\text{mW}$ here – energy flows more freely to small scales, leading to longer cascades, *i.e.*, cascades that extend to a viscous dissipation range at larger wavenumbers.

The IWT regime is brief and characterized by residual irregularities of the type found in DWT spectra that are imposed by discreteness. Slopes in the IWT regime are more easily discernible due to onset of KWT (recalling that IWT is defined as the intermediate regime that has both DWT and KWT behaviors, as previously discussed). At still higher powers, spectral volatility is mostly abated and the spectrum essentially has the smooth, continuous (linear in log–log space) appearance associated with KWT. In this regime, we expect Zakharov's kinetic theory [23] to hold to good approximation. However, one finds evidence of a constant spectral slope, with a slope value – approximately $-21/4$ – different than the $-17/4$ law theorized by Zakharov.

This is true despite the otherwise good agreement between the data and the characteristics of the kinetic theory in this regime. At even higher powers, the spectra depart from the constant −21/4 slope, signaling a change in regime from weak KWT to SWT. It is evident in Fig. 2(a) that SWT initially appears at higher wavenumbers and spreads towards lower wavenumbers as the power is increased.

The steepest spectral slope, −30/4, occurs twice over the range of investigated powers. Its first appearance is at the onset of continuous capillary wave motion. This is just beyond a range of input powers where the dynamics are intermittent and punctuated by brief quiescent periods. We do not study this low-power (non-stationary) intermittency range in this work. As the power increases beyond this onset value, the cascade remains truncated but its slope gradually increases to a maximum value that persists as the power is further increased to 24.3 mW. With a small subsequent increase in input power (∼ 1.5 mW) to 26.0 mW, the cascade abruptly completes, reinstating the initial slope of −30/4. This point in the noted spectra is obvious at the point of crossover of the indicated spectra in Fig. 2(b). This crossover occurs due to the truncation of the 24.3 mW spectrum into an elevated dissipation range at a wavenumber of roughly 10 krad/m, whereas the completed cascade continues with a steeper slope to a larger wavenumber of roughly 32 krad/m. If the power is further increased, the slope gradually increases to ≈ −21/4 and persists at this value up to an input power of 125 mW. Beyond 125 mW, the spectral slope again increases with an increase in power, approaching an apparently constant value of ≈ −2 in the SWT regime. This feature, which the authors are unable to compare with other studies from the literature, suggests a power-law type solution within a subset of the SWT regime. We note that the foregoing results differ from those obtained in simulations [40]. The slopes in the latter range from roughly −21/4 at lower powers to −17/4 at the highest powers and were obtained using Zakharov's kinetic equations modified to account for the discreteness of the domain.

3.2. Global nonlinearity analysis

For the purposes of bulk classification and inter-spectrum comparison, we define a single-value nonlinearity metric that is a weighted average of the same wavenumber-dependent nonlinearity measure that we used in the foregoing section (*i.e.*, for intra-spectrum analysis). At each wavenumber, the weighting is provided by a measure of three-wave dynamical correlation known as the bicoherence. Our bulk parameter is:

$$\delta_\mu = \sqrt{\frac{\sum_{n=0}^{N}\sum_{m=0}^{n}\bar{\delta}_n\,\bar{\delta}_m\,b_{n,m}^2}{\sum_{n=0}^{N}\sum_{m=0}^{n}b_{n,m}^2}}. \tag{10}$$

Here $\bar{\delta}_n = \delta_{\mathrm{NRB}}(\omega_n)/\delta_{k_n}$ quantifies nonlinearity at wavenumber k_n using the ratio of resonance broadening to eigenmode grid spacing. The weighting in Eq. (10) is provided by the bicoherence, $b_{n,m}$. Since bicoherence is defined over a symmetric frequency grid, we take double summation over unique pairings. The bicoherence is

$$b_{n,m} = \frac{|\langle\widetilde{\zeta}(t,f_n)\,\widetilde{\zeta}(t,f_m)\,\widetilde{\zeta}^*(t,f_n+f_m)\rangle_t|}{\langle|\widetilde{\zeta}(t,f_n)\,\widetilde{\zeta}(t,f_m)\,\widetilde{\zeta}^*(t,f_n+f_m)|\rangle_t}. \tag{11}$$

The sole difference between the numerator and denominator in this definition is in the order of operations between the time average $\langle\cdot\rangle_t$ and the modulus $|\cdot|$. The numerator is the bispectrum. In the bispectrum, phase information is removed after time averaging, such that this describes the average wave coupling strength at a particular point in frequency space. In the denominator of Eq. (11), the phases are set to zero (*i.e.*, made equivalent) before time averaging, representing perfect phase coupling. Thus, bicoherence, $b \in [0,1]$, measures the *normalized* three-wave coupling strength, and is specifically relevant for the analysis of capillary waves. Eq. (10) is similar to a metric used by Pan and Yue [40]. Since bicoherence obtained from Fourier methods is noisy and insufficient for use with turbulence spectra, we follow van Milligen et al. [50] in using wavelet-based transforms. The wavelet transforms $\zeta(t) \mapsto \widetilde{\zeta}(t,f)$ applied to the surface displacement measurements provides the instantaneous spectra needed to compute Eq. (11). Implementation details are provided in the [supplemental materials].

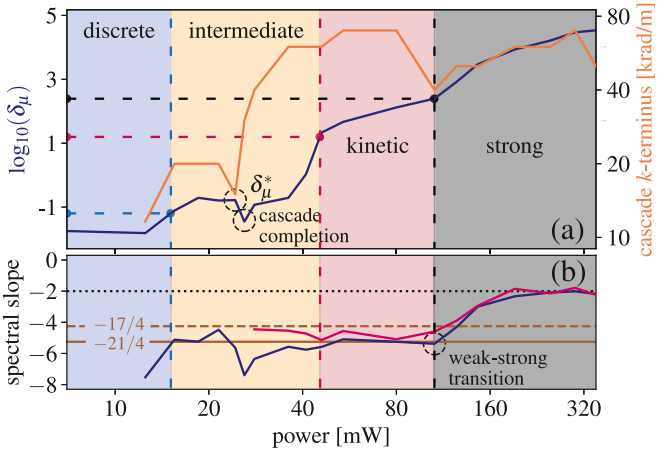

Fig. 3. Global nonlinearity map of variable-regime capillary WT. (a) Nonlinearity level Eq. (10) and terminal cascade wavenumber as functions of increasing input power. (b) Inertial regime spectral slope over (blue line) the entire cascade and (red line) the deep water regime. As the power continues to increase, a region of approximate constancy in nonlinearity, cascade length, and slope is observed just before the critical value, $\delta_\mu^* \approx 0.2$, beyond which a decrease of all three parameters occurs. A sharp increase in cascade length immediately follows $\delta_\mu^* \approx 0.2$. The KWT-SWT bound occurs when the spectral slope exceeds the experimentally constant value, −21/4, as observed within the kinetic regime. (For interpretation of the references to color in this figure legend, the reader is referred to the web version of this article.)

With Eq. (10) as our definition for the nonlinearity parameter, δ_μ, we find a non-monotonic structure that may be correlated to key features of the WT as provided in Fig. 3. The terminal cascade wavenumber and the spectral slope are plotted along with the nonlinearity parameter versus the input power. Since Zakharov's kinetic theory is based on assumptions of deep water waves and weak nonlinearity, the transition to strong nonlinearity is evident when the observed constant kinetic slope γ exceeds 21/4, and corresponding to a nonlinearity parameter value of $\mathcal{O}(\delta_\mu) = 10^2$. This suggests a boundary between weak and strong nonlinearity as follows:

$$\text{SWT} \quad \text{if} \quad \Lambda/10 \gg 1, \tag{12}$$

where Λ is obtained from Eq. (6b), Eq. (9b), or the interpolated region in between. Using this criteria, strongly nonlinear wave spectra have been identified in Fig. 2(a) in gray, appearing first at large wavenumbers, and spreading towards smaller wavenumbers as input power is increased.

Fig. 3 reveals many significant features beyond those already mentioned. At a 16 mW input – corresponding to the DWT-IWT bound – a region of approximately constant nonlinearity level, cascade length, and slope value exists. This region corresponds to the frozen turbulence region. This immediately precedes a critical value, $\delta_\mu^* \approx 0.2$, that causes cascade completion, as indicated by a very sharp increase in the terminal cascade wavenumber and an abrupt decrease in both δ_μ and slope. The entirety of the critical transitional process occurs within the IWT regime, during which the nonlinearity level "stalls", remaining approximately constant at $\delta_\mu \ll 1$.

The pattern of build-up, plateau, and decrease of the cascade k-terminus is initially repeated on entry to the KWT regime. However, the system enters into the SWT regime without significant decreases in the slope or nonlinearity level nor a sharp increase in the cascade's terminal wavenumber. On transition into the SWT regime, the changing slope resembles the pattern of slope change beginning at δ_μ^* and attains a new plateau of −2. This value of the slope may assume the same role in the SWT regime that the Zakharov slope assumes in the KWT regime.

3.3. Conclusions

Our analysis has shown that a thinly-wetted surface driven by high-frequency (1 MHz and beyond) ultrasonic forcing is a dynamically rich system. The dynamics traverse several wave turbulence regimes and, at sufficient powers, reach the strongly nonlinear regime. This regime is defined by spectral slopes that are much shallower than those predicted by weak wave turbulence theory. A region of slope constancy in the strong wave turbulence regime suggests the possibility of a corresponding solution to the governing equations. In atomizing systems, aerosol dispersal occurs at levels of nonlinearity that are inaccessible to modern wave turbulence theories, let alone classic interpretations of atomization based on Faraday systems and weakly turbulent phenomena. Further study of strongly nonlinear wave turbulence is therefore essential to a rigorous understanding of the atomization phenomenon.

CRediT authorship contribution statement

J. Orosco: Data curation, Formal analysis, Investigation, Methodology, Software, Validation, Visualization, Writing – original draft, Writing – review & editing. **W. Connacher:** Methodology, Visualization, Writing – review & editing. **J. Friend:** Conceptualization, Funding acquisition, Investigation, Methodology, Project administration, Resources, Software, Supervision, Visualization, Writing – review & editing.

Declaration of competing interest

The authors declare the following financial interests/personal relationships which may be considered as potential competing interests: James Friend reports financial support was provided by W M Keck Foundation. James Friend reports financial support was provided by Office of Naval Research.

Data availability

Data will be made available on request

Acknowledgments

We are grateful to the Office of Naval Research, United States (grant 12368098) and the W.M. Keck Foundation, United States for funding provided to J. Friend in support of this work. J. Orosco is grateful for support provided by the University of California's Presidential Postdoctoral Fellowship program. We are also grateful to Yves Emery and team at Lynceé Tec for assistance with adapting the DHM to this project's needs. Fabrication was performed in part at the San Diego Nanotechnology Infrastructure (SDNI) of UCSD, a member of the National Nanotechnology Coordinated Infrastructure, which is supported by the National Science Foundation (Grant ECCS–1542148).

Appendix A. Supplementary data

Supplementary material related to this article can be found online at https://doi.org/10.1016/j.chaos.2023.113615.

References

[1] Friend J, Yeo LY. Microscale acoustofluidics: Microfluidics driven via acoustics and ultrasonics. Rev Modern Phys 2011;83(2):647–704. http://dx.doi.org/10.1103/RevModPhys.83.647.

[2] Connacher W, Orosco J, Friend J. Droplet ejection at controlled angles via acoustofluidic jetting. Phys Rev Lett 2020;125(18):184504. http://dx.doi.org/10.1103/PhysRevLett.125.184504.

[3] Connacher W, Zhang N, Huang A, Mei J, Zhang S, Gopesh T, Friend J. Micro/nano acoustofluidics: Materials, phenomena, design, devices, and applications. Lab Chip 2018;18(14):1952–96. http://dx.doi.org/10.1039/C8LC00112J.

[4] Lang R. Ultrasonic atomization of liquids. J Acoust Soc Am 1962;34:6.

[5] Rajan R, Pandit A. Correlations to predict droplet size in ultrasonic atomisation. Ultrasonics 2001;39(4):235–55. http://dx.doi.org/10.1016/S0041-624X(01)00054-3, URL https://www.sciencedirect.com/science/article/pii/S0041624X01000543.

[6] Tsai SC, Lin SK, Mao RW, Tsai CS. Ejection of uniform micrometer-sized droplets from Faraday waves on a millimeter-sized water drop. Phys Rev Lett 2012;108:154501. http://dx.doi.org/10.1103/PhysRevLett.108.154501, URL https://link.aps.org/doi/10.1103/PhysRevLett.108.154501.

[7] Yuan S, Zhang Y, Gao Y. Faraday instability of a liquid layer in ultrasonic atomization. Phys Rev Fluids 2022;7:033902. http://dx.doi.org/10.1103/PhysRevFluids.7.033902, URL https://link.aps.org/doi/10.1103/PhysRevFluids.7.033902.

[8] Faraday M, XVII. On a peculiar class of acoustical figures; and on certain forms assumed by groups of particles upon vibrating elastic surfaces. Philos Trans R Soc Lond 1831;121:299–340. http://dx.doi.org/10.1098/rstl.1831.0018.

[9] Benjamin TB, Ursell FJ, Taylor GI. The stability of the plane free surface of a liquid in vertical periodic motion. Proc R Soc Lond Ser A Math Phys Sci 1954;225(1163):505–15. http://dx.doi.org/10.1098/rspa.1954.0218, https://royalsocietypublishing.org/doi/pdf/10.1098/rspa.1954.0218.

[10] Miles J. On rayleigh's investigation of crispations of fluid resting on a vibrating support. J Fluid Mech 1992;244:645–8.

[11] Kumar K. Linear theory of Faraday instability in viscous liquids. Proc R Soc Lond Ser A Math Phys Eng Sci 1996;452(1948):1113–26. http://dx.doi.org/10.1098/rspa.1996.0056, arXiv:https://royalsocietypublishing.org/doi/pdf/10.1098/rspa.1996.0056 URL https://royalsocietypublishing.org/doi/abs/10.1098/rspa.1996.0056.

[12] Qi A, Yeo L, Friend J. Interfacial destabilization and atomization driven by surface acoustic waves. Phys Fluids 2008;20:074103.

[13] Collignon S, Manor O, Friend J. Improving and predicting fluid atomization via hysteresis-free thickness vibration of lithium niobate. Adv Funct Mater 2018;28(1704359).

[14] Miles J. Nonlinear Faraday resonance. J Fluid Mech 1984;146:285–302.

[15] Miles J, Henderson D. Parametrically forced surface waves. Annu Rev Fluid Mech 1990;22(1):143–65.

[16] Bosch E, Lambermont H, van de Water W. Average patterns in Faraday waves. Phys Rev E 1994;49:R3580–3. http://dx.doi.org/10.1103/PhysRevE.49.R3580, URL https://link.aps.org/doi/10.1103/PhysRevE.49.R3580.

[17] Keolian R, Turkevich LA, Putterman SJ, Rudnick I, Rudnick JA. Subharmonic sequences in the Faraday experiment: Departures from period doubling. Phys Rev Lett 1981;47(16):1133–6.

[18] Blamey J, Yeo LY, Friend JR. Microscale capillary wave turbulence excited by high frequency vibration. Langmuir 2013;29(11):3835–45. http://dx.doi.org/10.1021/la304608a.

[19] Xia H, Shats M, Punzmann H. Modulation instability and capillary wave turbulence. Europhys Lett 2010;91(1):14002. http://dx.doi.org/10.1209/0295-5075/91/14002.

[20] Zhang Shuai, Orosco Jeremy, Friend James. Onset of visible capillary waves from high-frequency acoustic excitation. Langmuir 2023;39(10):3699–709.

[21] Sheremet A, Qin Y, Kennedy JP, Zhou Y, Maurer AP. Wave turbulence and energy cascade in the hippocampus. Front Syst Neurosci 2019;12:00062. http://dx.doi.org/10.3389/fnsys.2018.00062.

[22] Picozzi A, Garnier J, Hansson T, Suret P, Randoux S, Millot G, Christodoulides DN. Optical wave turbulence: Towards a unified nonequilibrium thermodynamic formulation of statistical nonlinear optics. Phys Rep 2014;542(1):1–132. http://dx.doi.org/10.1016/j.physrep.2014.03.002.

[23] Zakharov VE, Filonenko NN. Weak turbulence of capillary waves. J Appl Mech Tech Phys 1967;8(5):37–40. http://dx.doi.org/10.1007/BF00915178.

[24] Kartashova E. Nonlinear resonance analysis: theory, computation, applications. Cambridge: Cambridge University Press; 2010, http://dx.doi.org/10.1017/CBO9780511779046.

[25] Kleiner I. From Fermat to Wiles: Fermat's last theorem becomes a theorem. Elem Math 2000;55(1):19–37.

[26] Debnath L. Nonlinear water waves. Boston: Academic Press; 1994.

[27] Pushkarev AN, Zakharov VE. Turbulence of capillary waves theory and numerical simulation. Physica D 2000;135(1):98–116. http://dx.doi.org/10.1016/S0167-2789(99)00069-X.

[28] Connaughton C, Nazarenko S, Pushkarev A. Discreteness and quasiresonances in weak turbulence of capillary waves. Phys Rev E 2001;63(4):046306. http://dx.doi.org/10.1103/PhysRevE.63.046306.

[29] Nazarenko S. Sandpile behaviour in discrete water-wave turbulence. J Stat Mech 2006;2006(02):L02002. http://dx.doi.org/10.1088/1742-5468/2006/02/L02002.

[30] L'vov VS, Nazarenko S. Discrete and mesoscopic regimes of finite-size wave turbulence. Phys Rev E 2010;82(5):056322. http://dx.doi.org/10.1103/PhysRevE.82.056322.

[31] Kartashova E. Model of laminated wave turbulence. JETP Lett 2006;83(7):283–7. http://dx.doi.org/10.1134/S0021364006070058.

[32] Zakharov VE, Korotkevich AO, Pushkarev AN, Dyachenko AI. Mesoscopic wave turbulence. JETP Lett 2005;82(8):487–91. http://dx.doi.org/10.1134/1.2150867.

[33] Kartashova E. Discrete wave turbulence. Europhys Lett 2009;87(4):44001. http://dx.doi.org/10.1209/0295-5075/87/44001.

[34] Aubourg Q, Mordant N. Investigation of resonances in gravity-capillary wave turbulence. Phys Rev Fluids 2016;1(2):023701. http://dx.doi.org/10.1103/PhysRevFluids.1.023701.

[35] Brazhnikov MY, Kolmakov GV, Levchenko AA, Mezhov-Deglin LP. Observation of capillary turbulence on the water surface in a wide range of frequencies. Europhys Lett 2002;58(4):510. http://dx.doi.org/10.1209/epl/i2002-00425-9.

[36] Falcon É, Laroche C, Fauve S. Observation of gravity-capillary wave turbulence. Phys Rev Lett 2007;98(9):094503. http://dx.doi.org/10.1103/PhysRevLett.98.094503.

[37] Herbert E, Mordant N, Falcon E. Observation of the nonlinear dispersion relation and spatial statistics of wave turbulence on the surface of a fluid. Phys Rev Lett 2010;105(14):144502. http://dx.doi.org/10.1103/PhysRevLett.105.144502.

[38] Kharbedia M, Caselli N, Herráez-Aguilar D, López-Menéndez H, Enciso E, Santiago JA, Monroy F. Moulding hydrodynamic 2D-crystals upon parametric Faraday waves in shear-functionalized water surfaces. Nat Commun 2021;12(1):1130. http://dx.doi.org/10.1038/s41467-021-21403-0.

[39] Snouck D, Westra M-T, van de Water W. Turbulent parametric surface waves. Phys Fluids 2009;21(2):025102. http://dx.doi.org/10.1063/1.3075951.

[40] Pan Y, Yue DKP. Understanding discrete capillary-wave turbulence using a quasi-resonant kinetic equation. J Fluid Mech 2017;816:R1. http://dx.doi.org/10.1017/jfm.2017.106.

[41] Pan Y, Yue DKP. Direct numerical investigation of turbulence of capillary waves. Phys Rev Lett 2014;113(9):094501. http://dx.doi.org/10.1103/PhysRevLett.113.094501.

[42] Pan Y, Yue DKP. Decaying capillary wave turbulence under broad-scale dissipation. J Fluid Mech 2015;780:R1. http://dx.doi.org/10.1017/jfm.2015.487.

[43] Huang A, Connacher W, Stambaugh M, Zhang N, Zhang S, Mei J, Jain A, Alluri S, Leung V, Rajapaksa AE, Friend J. Practical microcircuits for hand-held acoustofluidics. Lab Chip 2021;21(7):1352–63. http://dx.doi.org/10.1039/D0LC01008A.

[44] Emery Y, Colomb T, Cuche E. Metrology applications using off-axis digital holography microscopy. Journal of Physics: Photonics 2021;3(3):034016. http://dx.doi.org/10.1088/2515-7647/ac0957.

[45] Vasan A, Connacher W, Friend J. Fabrication and methods of characterization of thickness mode piezoelectric devices for atomization and acoustofluidics. J Vis Exp 2020;162(e61015). http://dx.doi.org/10.3791/61015.

[46] Orosco J, Connacher W, Friend J. Data from: identification of weakly- to strongly-turbulent three-wave processes in a micro-scale system. UC San Diego Library Digital Collections; 2022, http://dx.doi.org/10.6075/J0WW7HVJ.

[47] Zakharov V. Statistical theory of gravity and capillary waves on the surface of a finite-depth fluid. Eur J Mech B 1999;18(3):327–44. http://dx.doi.org/10.1016/S0997-7546(99)80031-4.

[48] Zakharov VE, L'vov VS, Falkovich G. Kolmogorov spectra of turbulence I: wave turbulence. Springer Series in Nonlinear Dynamics, 1st ed.. Berlin, Heidelberg: Springer; 1992, http://dx.doi.org/10.1007/978-3-642-50052-7.

[49] Denissenko P, Lukaschuk S, Nazarenko S. Gravity wave turbulence in a laboratory flume. Phys Rev Lett 2007;99(1):014501. http://dx.doi.org/10.1103/PhysRevLett.99.014501.

[50] van Milligen BP, Hidalgo C, Sánchez E. Nonlinear phenomena and intermittency in plasma turbulence. Phys Rev Lett 1995;74(3):395–8. http://dx.doi.org/10.1103/PhysRevLett.74.395.